Euler–Lagrange Modeling of a Gas–Liquid Stirred Reactor with Consideration of Bubble Breakage and Coalescence

R. Sungkorn
Institute for Process and Particle Engineering, Graz University of Technology, A-8010 Graz, Austria

J. J. Derksen
Dept. of Chemical and Materials Engineering, University of Alberta, Edmonton, Alberta, Canada T6G 2G6

J. G. Khinast
Research Center Pharmaceutical Engineering, A-8010 Graz, Austria

DOI 10.1002/aic.12690
Published online July 5, 2011 in Wiley Online Library (wileyonlinelibrary.com).

Simulations of a gas–liquid stirred reactor including bubble breakage and coalescence were performed. The filtered conservation equations for the liquid phase were discretized using a lattice-Boltzmann scheme. A Lagrangian approach with a bubble parcel concept was used for the dispersed gas phase. Bubble breakage and coalescence were modeled as stochastic events. Additional assumptions for bubble breakup modeling in an Euler–Lagrange framework were proposed. The action of the reactor components on the liquid flow field was described using an immersed boundary condition. The predicted number-based mean diameter and long-term averaged liquid velocity components agree qualitatively and quantitatively well with experimental data for a laboratory-scale gas–liquid stirred reactor with dilute dispersion. Effects of the presence of bubbles, as well as the increase in the gas flow rate, on the hydrodynamics were numerically studied. The modeling technique offers an alternative engineering tool to gain detailed insights into complex industrial-scale gas–liquid stirred reactors.
 AIChE J, 58: 1356–1370, 2012
Keywords: computational fluid dynamics, lattice-Botlzmann method, immersed boundary condition, Lagrangian particle tracking, gas–liquid stirred reactor, bubble breakup and coalescence

Introduction

Stirred tank reactors are among the most widely used reactor types in a large variety of industrial processes involving multiphase flows. Typical examples include industrial hydrogenations or oxidations, as well as aerobic fermentation processes in which gas bubbles are dispersed in turbulent fluid flow induced by one or more impellers. In biotechnological processes, the activity and the growth of microorganisms (e.g., bacterial or fungal systems) or cells are sensitive to a number of parameters, such as dissolved oxygen content, substrate concentration, and pH level. A major challenge in these processes is to provide adequate liquid mixing and to generate a large interfacial contact area, while avoiding shear damage of microorganisms and cells caused by hydrodynamic effects.[1,2]

The flow structures in a single liquid-phase stirred reactor are known to be highly complex associated with time-dependent, three-dimensional phenomena covering a wide

Additional Supporting Information may be found in the online version of this article.

Correspondence concerning this article should be addressed to J. G. Khinast at khinast@tugraz.at.

range of spatial and temporal scales.[3] The complexity increases drastically when a gas phase is introduced. Additional effects include the interaction between phases in terms of mass, energy, and momentum exchange, the interaction between the second phase and the impeller, and interaction between bubble breakage and coalescence. As the reactor performance is a complex function of the underlying phenomena, a detailed knowledge regarding the hydrodynamics and the evolution of the dispersed phase is essential for the engineering of a high-performance reactor.

Traditionally, engineering of gas–liquid stirred reactors is based on empirical correlations derived from experiments. The information obtained from this approach is usually described in global parametric form and applicable within a narrow window of geometry configurations and operating conditions. Recently, the use of computational fluid dynamics (CFD) has gained some popularity among researchers and practitioners for the engineering of stirred reactors. Significant progress has been made over the last decades in the fields of turbulence and multiphase-flow modeling, numerical methods, and computer hardware. Consequently, time-dependent, three-dimensional simulations of gas–liquid stirred reactors with a sophisticated level of detail and accuracy are feasible today.

Various CFD modeling techniques for gas–liquid flows, where the gas phase is dispersed in the liquid phase, have been reported in the literature. These techniques can be grossly categorized based on their treatment of the dispersed phase into Euler–Euler (EE) and Euler–Lagrange (EL) approaches.[4,5] In the EE approach, both phases are treated as interpenetrating continua. The interactions between phases are modeled via the phase interaction terms that appear in the conservation equations describing the dynamics of the system. The EE approach assuming monodisperse spheres has been used in the works of Deen et al.,[6] Khopkar et al.,[7] and Zhang et al.[8] for simulations of gas–liquid stirred reactors. A more sophisticated EE approach, where the local bubble size distribution (BSD) is computed by solving population balance equations, has been reported by Venneker et al.,[9] Laakkonen et al.,[10] and Montante et al.[11,12] In the EL approach, each individual bubble or a parcel of bubbles is represented by a single point. The linear motion of the bubbles is governed by Newton's law of motion. Rotational momentum balances are typically not considered. The EL approach requires closure relations to account for the interphase forces, which can be obtained from empirical relations or from simulations with higher level of detail, for example, a front tracking approach[13] or volume of fluid methods. Closures for gas–liquid systems, which take into account the effect of high-gas-phase loadings are still an area of ongoing research (e.g., see Ref. 14). The EL approach is computationally expensive. However, the advantages of EL approach are its high flexibility with respect to incorporating microscopic and bubble-level phenomena, such as bubble–bubble interactions, bubble–wall interactions, breakup, and coalescence of bubbles. Simulations of gas–liquid stirred reactors using the EL approach are relatively rare in the literature. Some examples include the work of Wu et al.[15] and Arlov et al.[1] for simulations of reactors with monodisperse spheres and the work of Nemoda and Zivkovic[16] for the simulation of a reactor with bubble breakage.

The goal of this work is to assess the detailed modeling of a gas–liquid stirred reactor by an EL approach. The simulations are restricted to laboratory-scale reactors (with a volume in the order of 10 L) with dilute dispersion (i.e., a global gas-phase of up to 2% volume fraction). The reason for simulating these systems is that, in this work, we mainly focus on the validation of the modeling technique presented in the next section. Detailed validation requires highly resolved experimental information concerning liquid flow field and local BSDs, which are hard (if not impossible) to obtain in dense systems. Dispersed-phase volume fraction effects in the conservation equations of the continuous phase and high-frequency collisions drastically increase the complexity in denser systems, also from a computational point of view. The ability to numerically deal with denser systems is the subject of (our) current research. In engineering practice, the gas-phase fraction and the size of the reactor are typically much larger. However, as the presented modeling technique is based on elementary physical principles, which also play a role at the full-scale, the understanding of the underlying phenomena obtained in this work makes it worthwhile for researchers and practitioners. The main elements of the modeling technique used in our study are:

- The continuous liquid-phase is modeled using a variation of the lattice-Boltzmann (LB) scheme by Somers.[17] The LB scheme is used to solve the large-scale motions of the turbulent flow using the filtered conservation equations. The Smagorinsky subgrid-scale model is applied to model the effects of the subfilter scales.[18] It has been demonstrated that the scheme can accurately predict turbulent hydrodynamics in single phase system[3] as well as in multiphase systems.[19-21]
- An adaptive force-field procedure,[22] also known as an immersed boundary method, is used for describing the action of the reactor components (i.e., the impeller, tank wall, baffles, and internals) on the liquid flow field.
- The motion of the individual bubbles is computed by Lagrangian tracking taking into account the sum of forces due to stress gradients, net gravity, drag, lift, and added mass. The momentum transfer between phases, that is, the two-way coupling, is achieved by the mapping function with the virtual diameter concept introduced by Deen et al.[24] The impact of turbulence on the motion of the bubbles, that is, the fluctuations of the subfilter or residual fluid velocity along the bubble trajectory, is computed using the Langevin equation model introduced by Sommerfeld et al.[25]
- Collisions of bubbles are governed by the so-called stochastic interparticle collision.[26] Based on the stochastic model, coalescence of bubbles is determined by comparing the film drainage time with the bubble contact time.[27] Breakup of bubbles is accounted for using a theoretical model derived from the theory of isotropic turbulence.[28] It is assumed that breakup is caused mainly by the interaction of bubbles with turbulent eddies.

Although various elements of our approach have been reported in literature, the present modeling technique, for the first time, assesses the feasibility of using the LB scheme with the Lagrangian particle tracking model with consideration of bubble breakage and coalescence for simulations of gas–liquid stirred reactors. The simulations provide a detailed insight into gas–liquid stirred reactors with a high level of accuracy along with reasonable computational requirement.

In the next section, the modeling technique for turbulent bubbly flows in the EL framework will be briefly introduced.

A detailed discussion of this approach can be found in our previous work.[21] Additional models for the simulation of gas–liquid stirred reactors, for example, the treatment of reactor components, bubble breakup, and coalescence, will be discussed in detail. In the subsequent section, the model validation, ranging from a bubble column to a gas–liquid stirred reactor, will be presented and discussed in detail. The conclusion will be summarized in the final section.

Numerical Modeling Aspects

Liquid-phase hydrodynamics

In this work, the LB scheme is used to model the turbulent liquid flow. The LB scheme is based on a simple form of the Boltzmann kinetic equation, which can be used to recover the macroscopic hydrodynamic behavior of fluids.[29] The basic idea is that fluid flow, which is governed by conservation laws, can be simulated by a many-particles system obeying the same laws. A set of (fictitious) particles residing on a lattice moves to the neighbor sites and exchanges momentum (i.e., collide) with particles coming from other directions. The collision rules and the topology of the lattice are defined such that the Navier–Stokes equations are recovered.[30]

The specific LB scheme used here is based on the work by Somers[17] (see Refs. 3 and 31) with a cubic and uniform lattice. The scheme was chosen because of its robustness for turbulence simulations. This is due to the explicit treatment of the high-order terms, which results in enhanced stability at low viscosities and, thus, allows simulations of high Reynolds numbers. In the LB scheme, the arithmetic operations are local, that is, the data required for updating the flow in a grid point are obtained from its next neighbors and, specifically, the stress tensor is explicitly obtained from the data stored in a single node. Therefore, parallelization through domain decomposition requires only communication of subdomain boundary values, resulting in efficient parallel algorithms.

Gas–liquid flows in a bubble column or in a stirred reactor, are normally turbulent, even at laboratory scale and with gas volume fraction as low as 1%. Considering the liquid motions induced by dispersed gas bubbles, the turbulent stress can be divided into two components; one due to bubble buoyancy leading to liquid velocities above the turbulence onset and the other due to the so-called pseudo-turbulence caused by the fluctuation of the bubbles, that is, the zig-zagging motion of bubbles relative to the fluid, resulting in turbulent-like flows due to vortex shedding and interaction phenomena. Direct numerical simulation of these flows is not feasible due to limitation in computational resources, as the resolution of all length and time scales requires enormous amounts of grid cells and time steps. To overcome this limitation, only the evolution of the large-scale motions is resolved by applying a filtering process to the conservation equations of the liquid phase. The resolved flow can be interpreted as a low-pass filtered representation of the real flow. The impact of the residual motion that resides at scales smaller than the filter width is modeled using the subgrid scale (SGS) model by Smagorinsky.[18] In this model, the SGS motion is considered to be purely diffusive, and the model only drains energy from the resolved motions without feedback. A larger fraction of the eddies and more of the energy residing in the flow are resolved with a finer grid spacing, that is, a higher resolution. However, the choice of grid spacing in the EL approach is also restricted by the size of the bubbles, as will be discussed in detail in the next section. Furthermore, Hu and Celik[32] pointed out that the residual motion of the pseudo-turbulence, which posses a universal energy spectrum different from the classical $-5/3$ decay in single phase turbulence, could (in principle) be captured using a dedicated SGS model. Such a reliable and accurate SGS model for multiphase flows is not available. Therefore, the SGS model used in this work is adopted directly from the single-phase SGS model. This is justified by our favorable results in relation to experimental data as will be shown later in this work. The eddy viscosity V_t concept is used to represent the impact of the SGS motion as:

$$v_t = (C_S \Delta)^2 \sqrt{S^2}, \tag{1}$$

with the Smagorinsky constant C_S, the filter width Δ (equal to the cubic grid cell size h), and the resolved deformation rate $\sqrt{S^2}$. The value of C_S is kept constant at 0.10 throughout this work. It has been demonstrated that the variation of C_S has only marginal effect on the predicted flow field.[21,33]

As the simulations discussed here are restricted to dilute dispersions, that is, global gas volume fractions of up to 2%, it can be assumed that the void fraction term in the momentum conservation equations for the liquid phase has a relatively small effect on the flow. The filtered conservation equations (with source terms representing forces exert by the bubbles and the reactor components) for single phase flow are approximately valid. The formulation and detailed discussion for the conservations equations used in this work can be found in Refs. 3 and 31. This assumption has been successfully used for simulations of multiphase flows within the dilute dispersion limit by several researchers (e.g., see Refs. 19, 32, and 21).

Impeller and tank wall treatment

Stirred tanks typically consist of a cylindrical vessel equipped with one or more impellers, baffles, and, optionally, other internals. They can be divided, into static (i.e., tank wall, baffles, and internals) and moving components (i.e., impellers and shaft). In this work, an adaptive force-field technique, also known as an immersed boundary method,[22,34] is used to describe the action of the reactor components on the liquid flow field. The method mimics these components by a set of control points on their surface. It computes forces on the flow such that the flow field has prescribed velocities at the control points within the domain, that is, equal to zero at static components and equal to the surface velocity for the moving components. The deviation from the prescribed velocities is estimated by a second-order interpolation and imposed back on the lattice sites during the collision step.[3]

In the vicinity of walls, the turbulence becomes anisotropic, that is, fluctuations in the wall-normal direction are suppressed. Consequently, the SGS Reynolds stresses should become zero. These effects are accounted by using the Van Driest wall damping function[35] with the universal velocity profiles.[36]

Bubble dynamics

The dispersed phase (i.e., the bubble phase) is tracked in a Lagrangian manner. A point-volume (also known as point-force) assumption is used. In this assumption, the bubble is assumed to have a spherical shape, and the bubble surface effect on the continuous fluid is neglected.[5] Each point representing a parcel of bubbles with identical properties (i.e., position, velocity, and diameter) is tracked simultaneously in the time-dependent, three-dimensional flow field. It is noted that the number of bubbles in a parcel is a real number $\{\Re\}$. Its trajectory is computed based on Newton's law of motion. All relevant forces, such as net gravity force, forces due to stress gradient, drag, net transverse lift, and added mass force are considered. Thus, the following set of equations will be solved for the motion of bubbles in a parcel:

$$d_t \mathbf{x}_p = \mathbf{u}_p, \tag{2}$$

$$\rho_p V_p d_t \mathbf{u}_p = \left(\rho_p - \rho_l\right) V_p g + \rho_l V_p D_t \mathbf{u} - \frac{1}{8} C_D \rho_l \pi d_p^2 \left|\mathbf{u}_p - \mathbf{u}\right| \left(\mathbf{u}_p - \mathbf{u}\right) - C_L \rho_l V_p \left(\mathbf{u}_p - \mathbf{u}\right) \times \nabla \times \mathbf{u} - C_A \rho_l V_p \left(D_t \mathbf{u}_p - D_t \mathbf{u}\right) \tag{3}$$

with χ_p being the centroid position of the parcel, u_p the velocity, ρ_p the bubble density, V_p the bubble volume with the diameter d_p, $\mathbf{g}$ the gravitational acceleration, ρ_l the liquid density, and $\mathbf{u}$ the liquid velocity at $\mathbf{X}_p$. The drag C_D and lift C_L coefficients depend on the bubble Reynolds number $Re_p = \left|\mathbf{u}_p - \mathbf{u}\right| d_p / \nu_l$ and the Eötvös number $Eo = \left(\rho_l - \rho_p\right) |g| d_p^2 / \sigma$. The added mass force coefficient C_A is assumed to be constant at 0.5. Expressions for the forces acting on a bubble and its coefficients are summarized in the Appendix. Note that because the buoyancy force has been already included in the net gravity force, the forces due to stress gradient in the fluid include only the dynamic pressure and the deviatoric stress gradient. Hence, the forces due to the fluid stress gradient can be reformulated in term of the fluid acceleration as shown in Table A1.[23,32] The liquid velocity $\mathbf{u}$ at the centroid of the parcel in Eq. (3) consists of the resolved liquid velocity $\bar{\mathbf{u}}$ and a (residual) liquid fluctuating component $\tilde{\mathbf{u}}$. The latter component is used to mimic the impact of turbulence on the motion of the bubble, that is, the fluctuations of the subfilter (residual) liquid velocity along the bubble trajectory.

The interpolation of the liquid properties on the Eulerian grid nodes to the centroid of the parcel on the Lagrangian reference frame (and vice versa) is achieved using a "cheap clipped fourth-order polynomial" mapping technique proposed by Deen et al.[24] (see Appendix for the formulation). In principal, the mapping function ς evaluates a property, such as the liquid velocity at the parcel centroid, by the integration of the liquid velocity at the Eulerian grid nodes that is located inside a predefined influence diameter (set to $2d_p$ in this work). Forces exerted by a parcel on the Eulerian grid nodes are accounted for via the interphase force terms in the conservation equations $\mathbf{F}_{p \to l}$, that is, the back coupling. The force terms consist of the drag $\mathbf{F}_D$, lift $\mathbf{F}_L$, and added mass forces $\mathbf{F}_A$ as a function of the mapping function ς and the number of bubbles in the parcel n_p. At a grid node j with volume $V_{cell,j}$, the forces exerted by a parcel **i**can be expressed as:

$$\mathbf{F}_{p,i \to l,j} = -\frac{\varsigma_j \, n_p}{V_{cell,j}} \left(\mathbf{F}_D + \mathbf{F}_L + \mathbf{F}_A\right). \tag{4}$$

As mentioned earlier, a larger fraction of the eddies (and more of the energy residing in the flow) can be resolved using a higher grid resolution. Thus, a more accurate prediction of turbulent flow hydrodynamics requires finer grid spacing. In the framework of the EL approach, it is, however, suggested that the grid spacing ratio to the bubble diameter h/d_p should be greater than unity to maintain the validity of the point-volume approach. Therefore, the h/d_p value used here should compromise between a sufficiently fine grid resolution to capture the most energetic eddies and a sufficiently coarse grid resolution to keep the point-volume assumption valid. However, we relax this restriction by allowing the h/d_p value to be lower than unity but greater than 0.5. This allows us to include large bubbles (with a diameter greater than the grid spacing) that are present mostly at the sparger and close to the impeller shaft. Note that the volume of parcels with large bubble is lower than 10% of the total bubble volume (and the number of large-bubble parcels is less than 1% of the total number of bubbles) having only a minor effect on the resolved flow field. The applicability of a h/d_p value less than unity has been demonstrated by Darmana et al.[37] and is justified by favorable results obtained in this work.

Collisions

Collisions between bubbles can be analyzed using direct collision models, for example, soft sphere[38] and hard sphere collision models,[39] or statistics-based collision models, for example, the stochastic interparticle collision model.[26] In this stochastic model, no direct collisions, where a large amount of information from surrounding bubbles is required, are considered. Instead, only a fictitious collision partner (i.e., parcel) is assumed and a collision probability according to kinetic theory is established for each parcel at each time step of the trajectory calculation. The bubble size and velocity of the fictitious parcel are randomly generated based on the statistic information (with Gaussian distribution) regarding BSD and velocity collected at Eulerian grid nodes. The fictitious parcel consists of bubbles with identical properties and similar number as in the considering parcel. Hence, the bubbles in the fictitious parcel can be considered as a representative for the surrounding bubbles. The collision probability P_{coll} is calculated based on the properties of the parcel (and its collision partner) and the local fluid properties as:

$$P_{coll} = \frac{\pi}{4} \left(d_p - d_{fict}\right)^2 \left|\mathbf{u}_p - \mathbf{u}_{fict}\right| n_p \Delta t, \tag{5}$$

where the subscript fict represents properties of the bubbles in the fictitious parcel. The occurrence of a collision between a parcel and a fictitious parcel is determined by a comparison between the probability with a uniform random number in the interval [0,1]. The collision can result in momentum exchange (bouncing) or coalescence between the bubbles in the parcels. In case of a bouncing collision, the impact point is statistically determined on a collision cylinder where the fictitious parcel is stationary. A detailed description of the stochastic interparticle collision procedure can be found in the work of Sommerfeld.[26] The procedure to determine coalescence of bubbles will be described in the next section.

Collisions between a parcel and the surfaces (tank, baffles, and impeller) are considered to be elastic and frictionless. As the motion of the moving components (e.g., impeller shaft, blades, and disc) is rotational, a collision with these components adds momentum to the bubble resulting in a change of the bubble tangential velocity[19]:

$$u_{p,\theta,out} = -u_{p,\theta,in} + 2\,r_p\Omega, \tag{6}$$

where $u_{p,\theta,out}$ and $u_{p,\theta,in}$ represent the tangential velocity after and before the collision, respectively. The local velocity at the impact point $r_p\Omega$ is the product of the angular velocity $\Omega = 2\pi N$ (with N being the impeller rotational speed) and the distance from the center axis r_p. At impact, the distance between a parcel and a solid component is calculated based on the effective radius, r_{eff}, of a parcel bubble as

$$r_{eff} = \left(\frac{3n_pV_p}{4\pi}\right)^{1/3}, \tag{7}$$

with n_p being the number of bubbles in the parcel and V_p being the bubble volume.

Coalescence model

Following a collision between a parcel and a fictitious parcel described in the previous section, coalescence between the bubbles in parcel and the bubbles in the fictitious parcel is determined using the approach introduced by Prince and Blanch.[40] In this approach, coalescence will take place when the bubble contact time τ_{ij} is greater than the film drainage time t_{ij}. Otherwise, a rebound occurs. It is assumed that, in the frame of the considered Lagrangian collision model, the contact time can be expressed by:

$$\tau_{ij} = \frac{C_C R_{ij}}{u_n}, \tag{8}$$

with the equivalent bubble radius R_{ij}

$$R_{ij} = 2.0\left(\frac{2}{d_p} + \frac{2}{d_{fict}}\right)^{-1}, \tag{9}$$

where u_n is the relative approaching velocity in normal direction, C_C is the deformation distance as a fraction of the effective bubble radius; its value of 0.25 gives the best agreement with the experimental data[27] and is used throughout this work. Neglecting the effects due to surfactants and Hamaker forces, the film drainage time can be expressed as:

$$t_{ij} = \sqrt{\frac{R_{ij}^3\rho}{16\,\sigma}}\,\ln\left(\frac{h_0}{h_f}\right), \tag{10}$$

with the initial film thickness h_0 for air-water set to 0.1 mm, the final film thickness before rupture h_f set to 0.01 μm,[40] and the surface tension σ. The properties of the new bubble after coalescence are calculated from a mass and momentum balance. The new bubble diameter after coalescence is calculated as

$$d_{p,new} = \left(d_{p,old}^3 + d_{fict}^3\right)^{1/3}. \tag{11}$$

As the total volume of the parcel must be conserved, the number of bubbles in a parcel after coalescence is expressed as

$$n_{p,new} = n_{p,old}\left(\frac{d_{p,old}}{d_{p,new}}\right)^3. \tag{12}$$

Based on the collision cylinder where the fictitious parcel is stationary, only the bubble normal velocity to the bubble in the fictitious parcel is changed, while the other velocity components remain unchanged. Thus, the normal velocity after coalescence $u_{p,n,new}$ can be expressed as

$$u_{p,n,new} = u_{p,n,old}\left(\frac{d_{p,old}^3}{d_{p,old}^3 + d_{fict}^3}\right). \tag{13}$$

It is important to emphasize here that a coalescence of bubbles takes place between a (real) parcel and a fictitious parcel, not between two real parcels. In the case of bouncing collisions (the contact time less than the drainage time), the normal velocity after collision is a function of the coefficient of restitution α (set to 0.90 in this work) and can be described by:

$$u_{p,n,new} = u_{p,n,old}\left(\frac{d_p^3 - \alpha\, d_{fict}^3}{d_p^3 + d_{fict}^3}\right). \tag{14}$$

Breakup model

A breakup model proposed by Luo and Svendsen[28] is used in our work. The model was derived from the theories of isotropic turbulence and contains no adjustable parameters. The bubble interaction with turbulent eddies is assumed to be the dominant breakup mechanism. It is further assumed that only the eddies of length scale smaller than or equal to the bubble diameter participate in the breakup mechanism. Larger eddies simply transport the bubble without causing breakup. The breakup rate of bubbles with volume V_p into volumes of $V_p f_{BV}$ and $V_p\,(1 - f_{BV})$ when being in contact with turbulent eddies in the size range of λ_{min} to d_p can be expressed as:

$$\frac{\Omega_B\left(V_p : V_p f_{BV}\right)}{\left(1-\alpha_g\right)n_p} = 0.923\left(\frac{\varepsilon}{d_p^2}\right)^{1/3} \int_{\xi_{min}}^{1} \frac{(1+\xi)^2}{\xi^{11/3}}\exp\left(-\frac{2c_f\sigma}{\rho\,\varepsilon^{2/3}\,d_p^{5/3}\,\xi^{11/3}}\right)d\xi, \tag{15}$$

where α_g is the gas phase volume fraction, ε is the energy dissipation at the centroid of the parcel, and $\xi_{min} = \lambda_{min}/d_p$. The breakage volume fraction f_{BV} is calculated from:

$$f_{BV} = 0.5 + 0.5\tan\,h\left(10\,\frac{(RN - 0.5)}{\pi}\right), \tag{16}$$

where RN is an uniform random number with the interval [0,1]. The resulting volume fraction of the daughter bubbles has a U-shaped distribution, that is, the breakup into equal size has the lowest probability, while the breakup into infinitesimal volumes has the highest probability. In this work, we limit the range of breakage volume fraction in the interval [0.2,0.8]. Accordingly, the increase coefficient of surface area c_f is expressed as:

$$c_f = f_{BV}^{2/3} + (1 - f_{Bv})^{2/3} - 1. \tag{17}$$

The minimum size of eddies in the inertial subrange of isotropic turbulence λ_{min} is assumed to be proportional to the length of the Kolmogorov-scale eddies λ_{ms}:

$$\lambda_{min} = 11.4\,\lambda_{ms}, \tag{18}$$

with

$$\lambda_{ms} = \left(\frac{v^3}{\varepsilon}\right)^{1/4}, \tag{19}$$

where v is the liquid-phase kinematic viscosity.

In this work, the breakup rate is considered to be a stochastic value determined from a randomly generated breakage volume fraction given in Eq. 16. Thus, the breakup of a parcel within a certain interval is decided in the similar manner as for the collision of bubbles, that is, by comparison with a uniform random number in the interval [0,1]. Furthermore, it is assumed that the breakup only takes place within the parcel and will not result in a new parcel. Instead, it will result in a parcel with a new bubble diameter calculated according to the breakage volume fraction. The number of bubbles in a parcel after breakup is calculated using Eq. 12. Regardless of the success of the breakup, the parcel is assumed to interact with certain eddies in a certain interval characterized by the particle–eddy interaction time t_e. The next estimation of the breakup rate will be carried out after t_e s, see Appendix for the formulations. This assumption is very important for a system where a high level of turbulence is present, for example, in a stirred reactor. It prevents unphysical consecutive breakups of bubbles and provides a time-step resolution-independent solution.

Results and Discussion

Bubble column with monodisperse bubbles

Dispersed gas–liquid flows in three-dimensional (non-stirred) bubble columns have been studied experimentally by several groups, including Deen et al.[41] and Van den Hengel et al.[42] Coalescence of bubbles was inhibited by adding salt solution resulting in a bubble column with (approximately) uniform bubble size. As their data are used to validate our model, we neglected breakup and coalescence of bubbles in this part of the study. Fluid flow was induced mainly by bubbles where the motion of bubbles relative to the liquid resulted in turbulent-like flow. The bubble plume fluctuated only weakly at the lower part of the column and was meandering around the column at the upper part. This fluctuation was caused by various mechanisms including, most importantly, bubble–bubble collisions and turbulence.

Modeling of these bubble columns was reported by Sungkorn et al.[21] Their predicted mean and fluctuating liquid velocity components were in good agreement with the experimental data of Ref. 41 cited above. Sensitivity to grid size over bubble diameter ratio h/d_p was also studied by performing simulations with a h/d_p-value of 1.10, 1.25, and 1.50. The study concluded that a finer grid (i.e., a lower h/d_p value) provides a better agreement with the experiment, while the coarsest grid was not sufficient to correctly capture the features of the flow field.

In the present work, we study the sensitivity of the predictions when a h/d_p-value lower than unity is used. It is worth to emphasize that in the EL approach considered here, a point-volume assumption is used and that the bubbles' surface effect on the continuous fluid flow is neglected. We relax the assumption by further assuming that a h/d_p-value less than unity (but greater than 0.5) can be used and will not drastically violate the point-volume assumption. This additional assumption will be justified by the favorable results obtained here.

The bubble column considered has a square cross-section with a width, depth and height of 0.15, 0.15, and 0.45 m, respectively. Air bubbles are introduced at the bottom-center plane with an area of 0.03×0.03 m^2 and with a superficial gas velocity of 4.6 mm/s. A bubble mean diameter of the order of 4 mm was observed in the experiments.[41] Bubbles were assumed to have uniform size in this work. To verify the validity of a model with a h/d_p-value less than unity, a simulation with a h/d_p value of 0.75 was carried out and compared with the simulation results reported by Sungkorn et al.[0] for a h/d_p value greater than unity.

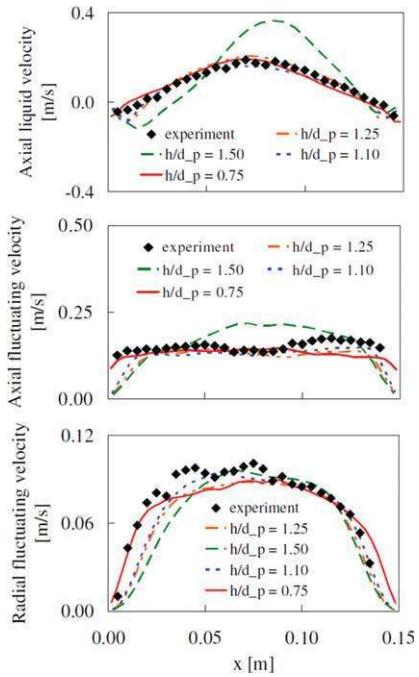

Figure 1. Comparison of the predicted and experimental long-term averaged liquid velocity and fluctuating velocity components with various grid size to bubble diameter ratios h/d_p at a height of 0.28 m and a depth of 0.075 m.

[Color figure can be viewed in the online issue, which is available at wileyonlinelibrary.com.]

The domain was discretized by a uniform cubic grid of $50 \times 50 \times 150$ lattices in width, depth, and height, respectively. This resulted in a bubble size of 1.5 times the lattice distance. A no-slip boundary condition was applied at the walls, except for the top where a free-slip boundary condition was applied. Bubble parcels were injected at the bottom of the column and left the simulation domain once they touched the top surface. In this case, due to the low gas-phase fraction, one parcel contained only one bubble. The calculation started with a quiescent liquid and proceeded for 150 s with a time step for the liquid phase of 10 μs. A sub-time step of 1 μs was used for the calculation of the bubble motion. To obtain statistically meaningful data, the averaged quantities were computed from 20 to 150 s.

A comparison between the simulations with various h/d_p values and measured data is shown in Figure 1. As can be seen in Figure 1a, the averaged vertical velocity profile is accurately reproduced in all cases except for a h/d_p value of 1.50. Similarly, the fluctuating components of the resolved flow field were correctly captured by all simulations except, again, for a h/d_p value of 1.50. This might be attributed to an insufficient resolution when a grid too coarse is used. As can be seen, the use of a h/d_p value of 0.75 improves the

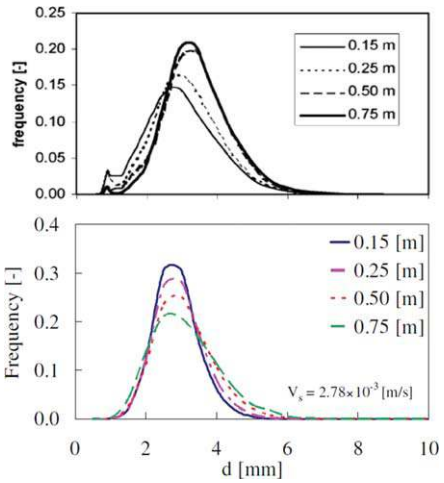

Figure 2. Comparison of the experimental (a) and the predicted (b) bubble size distribution at various heights with the superficial gas velocity of 2.78 × 10^{-3} m/s.

The simulation was performed with a BSD with a mean diameter of 2.5 mm at the nozzle. [Color figure can be viewed in the online issue, which is available at wileyonlinelibrary.com.]

predictions, especially at the region near the wall. This is because, with a finer grid resolution, a larger fraction of the eddies and, consequently, more of the energy residing in the flow are resolved. These favorable results show that the use of a h/d_p value lower than unity in this case will not deteriorate the simulation, at least in the prediction of the flow field. However, it is important to note that the refinement of the grid also results in an increase of computational cost: reducing the (uniform) grid spacing by a factor q increases the grid size with a factor q^3 and (due to explicit time stepping) the computational effort by q^4.

Bubble column with inclusion of breakage and coalescence

A pseudo-two-dimensional bubble column has been used to study the effect of superficial gas velocity on the BSD by Van den Hengel et al.[42] The underlying phenomena are similar to the bubble column discussed earlier with the additional complexity due to bubble coalescence. The dimensions of the bubble column are 0.20, 0.03, and 1.40 m, in width, depth, and height, respectively. Air bubbles were injected at the mid-bottom from a nozzle with a diameter of 0.02 m with a gas superficial velocity of 1.39 × 10^{-3}, 2.78 × 10^{-3}, and 4.17 × 10^{-3} m/s. It was reported in their work that the bubbles at the nozzle had a size distribution around 3 mm.

In our study, the fluid domain was discretized on a uniform cubic grid of 40 × 6 × 280 lattices in width, depth, and height, respectively. The other simulation settings were similar to the previous simulation case. Gaussian-shape BSDs with a mean diameter of 2.5 and 3 mm (corresponding to a bubble size of 0.5 and 0.6 times the lattice distance, respectively) and a variance of 0.25 mm were generated at the nozzle. Breakup and coalescence of bubbles were taken into account. Because of the restriction of the h/d_p value discussed earlier, coalescence will only take place with a bubble smaller than 2.0 times the lattice spacing and, similarly, breakup will only take place with a bubble larger than 0.1 times the lattice spacing. The long-term averaged results were based on results between 20 and 150 s.

Figure 2 shows the measured and predicted long-term averaged BSD at various heights. It can be observed from the experimental data that the mean bubble diameter and the BSD slightly shifted to the right side, that is, to bigger diameters, caused by bubble coalescences. A similar behavior is obtained in the simulations. Although the agreement is quite good, there exist, however, some deviations in the BSD profiles. Similar deviations were also obtained in the simulations of Van den Hengel et al.[42] One reason for this observation may be the resolution of the measurement and/or the lack of accurate BSD data at the nozzle (i.e., at the air inlet). The latter explanation is also supported by the fact that in the experiment a bimodal BSD is observed.

Figure 3 shows the number mean diameter at various heights with different superficial gas velocities. The sensitivity of the BSD with respect to the sparger (initial) BSD was studied by using initial BSDs with mean diameters of 2.5 and 3 mm. At low superficial gas velocities (i.e., 1.39 × 10^{-3} and 2.78 × 10^{-3} m/s), good agreements for the number mean diameter d_{10} along the axial direction were obtained with the initial BSD of 2.5 mm. However, the simulation with the initial BSD of 3.0 mm provides a good agreement with the experiment at a higher superficial gas velocity (i.e., 4.17 × 10^{-3} m/s). This behavior may be explained by the well-known fact that the initial bubble size at the sparger increases with increasing superficial velocity.[10] Furthermore, also immediate

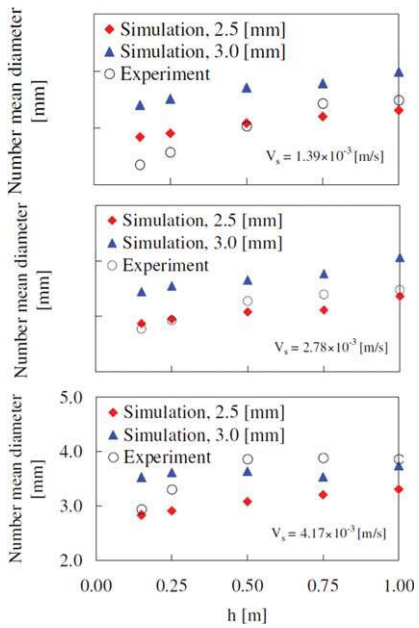

Figure 3. Comparison of predicted and experimental number-mean diameters at various heights using different initial bubble diameters and gas superficial velocities (all diagrams have the same *y*-axis scale).

[Color figure can be viewed in the online issue, which is available at wileyonlinelibrary.com.]

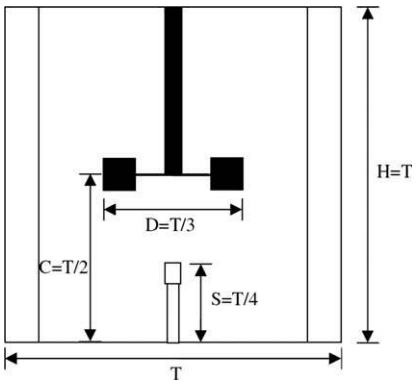

Figure 4. Geometry of the stirred reactor with a Rushton turbine and a tube sparger.

coalescence at the sparger occurs. This, again, highlights the importance of knowing the initial BSD at the sparger for an accurate prediction. Although the initial bubble size can be roughly estimated using, for example, the model proposed by Geary and Rice,[43] detailed information concerning the sparger is essential, yet rarely available in literature.

Gas–liquid stirred reactor

Detailed experimental investigations of a gas–liquid stirred reactor were reported by Montante et al.[11,12] and were used for validation of our method. In their work, image analysis was used to collect data concerning liquid flow field and the BSD at the mid-plane between the baffles. The reactor had a standard configuration consisting of a cylindrical, flat-bottomed, baffled tank with diameter $T = 23.6$ cm and the liquid filled-level $H = T$. The reactor was equipped with a Rushton turbine with a diameter $D = T/3$, at the center of the reactor C = T/2. The geometry of the reactor is depicted in Figure 4. The working fluid was water with a viscosity $v$of 1.0×10^{-6} m^2/s and density ρ of 1.0×10^3 kg/m^3. The impeller rotational speed N was fixed at 450 rpm throughout the study, corresponding to a blade tip speed of 1.85 m/s and a Reynolds number, defined as $Re = ND^2/v$, of $\sim$ 46,000. Air bubbles were injected into the system via a sparger made of a tube of 3.3 mm diameter with a porous membrane on top. The sparger had a distance of T/4 from the bottom. The gas flow rate was varied from 0.02, 0.05, to 0.07 vvm. The reactor operated in the complete dispersion regime.[11]

For the simulations, a cubic computational grid of 85^3 lattice cells was defined. A no-slip boundary condition was used at all faces except for the top surface, where a free-slip boundary condition was defined to represent the free surface. Sets of control points, representing the cylindrical wall, the baffles, the impeller, the impeller shaft, and the sparger tube, were generated inside the computational domain according to the forcing algorithm introduced earlier. In the simulations, a grid spacing h equal to 2.9×10^{-3} m was used. The diameter of the impeller had a size of 27 times the grid spacing. The distance between two control points at the impeller surface was $0.7h$. Similar strategy was used to represent the other parts. The total number of control points in the domain was 33,000. The simulations started with the reactor at rest and proceeded with a time step for the liquid phase of 20 μs and a subtime step of 4 μs for the calculation of the bubble motion. Thus, the impeller completes a full revolution in 6667 time steps. At any given moment, for example, in Case 5, the simulation has $\sim$ 1300 parcels, corresponds to 90,000 bubbles and global gas holdup of 0.4% (also Montante et al.[12] report gas holdups below 1%). After 30 impeller revolutions, the data of the liquid flow field and the BSD were collected for the following 60 revolutions and statistically analyzed. The wall-clock time for one impeller revolution was $\sim$ 1.5 h when 4 Intel® Xeon® E5540 (at 2.53 GHz) processors were used. This averaging period was shown to be sufficiently long for generating statistically meaningful results. An overview of the simulation cases is shown in Table 1. Note that the initial bubble diameter used in the simulations was greater than the grid spacing, that is, a h/d_p value less than unity. For example, an initial diameter of 4 mm results in a h/d_p value of 0.74. As will be shown later, the significant bubble breakup occurs in the impeller region, resulting in much smaller bubbles. Hence, only 1% of the bubbles or less in the reactor have a diameter greater than the grid spacing.

First, the influence of the initial bubble diameter on the simulation results was studied. Two simulations were carried out: one with an initial bubble diameter of 4 mm (Case 1) and another one with a Gaussian BSD distribution with a mean diameter of 3.5 mm and variance of 0.5 mm (Case 2). The gas flow rate was set to 0.02 vvm in both cases. Figure 5 shows the measured and predicted long-term averaged local number-mean diameter d_{10} in the reactor. Note that the predicted d_{10} shown here is a angle-averaged value. The trend and magnitude of the predicted d_{10} in both cases agrees fairly well with the measured data. In Case 1, the simulations slightly over-predicted d_{10} in the impeller regime and slightly under-predicted the diameter in the rest of the reactor. In contrast, the predicted d_{10} in Case 2 agrees well with the measured data in most parts, except in the impeller regime where the d_{10} is over-predicted. This, again, highlights the importance of initial bubble size accuracy of the simulation. To reduce the parameters that will influence the prediction and for the simplicity of the study, a uniform initial bubble size of 4 mm was used for the rest of the study.

A comparison between the predicted (Case 1) and the measured cumulative size distribution (CSD) of bubble at the lower and upper part is shown in Figure 6. The predicted CSD was calculated by dividing the diameter between 0.0 and 4.5 mm into 15 classes and counting the frequency of bubbles in each class. As can be seen, the predicted CSD distribution agrees very well with the measured data. Deviation can be observed in the regime of small bubbles. This could be due to many reasons, for example, in the break up model, where the daughter size distribution is governed by

Table 1. Overview of the Stirred Tank Simulation Cases

Case	N (rpm)	Qg (vvm)	Initial dp (mm)
1	450	0.02	4.0
2	450	0.02	Mean = 3.5/Variance = 0.5
3	450	0.0	-
4	450	0.05	4.0
5	450	0.07	4.0

the U-shape distribution [Eq. (16)] in which the probability of very small and very large daughter sizes is the highest. Thus, other daughter size distributions, such as an M-shape distribution,[44] may be used to improve the prediction. It is also important to note that the smallest detectable bubble in the experiment of Montante et al.[12] was 0.3 mm, whereas in the simulation, the smallest allowable bubble was $\sim$ 0.25 mm and was included in the first cumulative class.

On the basis of good agreement between experiment and simulation for the dispersed phase, we further examined the quality of the prediction of the liquid flow field. Predicted and experimental axial and radial long-term averaged liquid velocity components along the radial direction at various heights are shown in Figure 7. As can be seen, a quite good agreement between the predicted and measured data is achieved at all considered heights. The radial velocity profiles changes only slightly along the radial direction. A significant change in magnitude can be seen at the height of the impeller where a strong outflow exists ($z/T = 0.49$) as the configuration corresponds to a radially discharging impeller. In contrast, the axial velocity profiles change in magnitude and sign along the radial direction at all elevations. Also, a very good agreement is achieved for the long-term averaged velocity components along the axial direction at various radial positions, see Figure 8. A jet-like radial outflow has the highest magnitude close to the impeller and decreases with further distance from the impeller. The axial velocity component changes its magnitude along the axial direction and radial position according to flow recirculation generated by the Rushton turbine. Slight deviations can be noticed for the radial velocity component at the peak of the impeller jet.

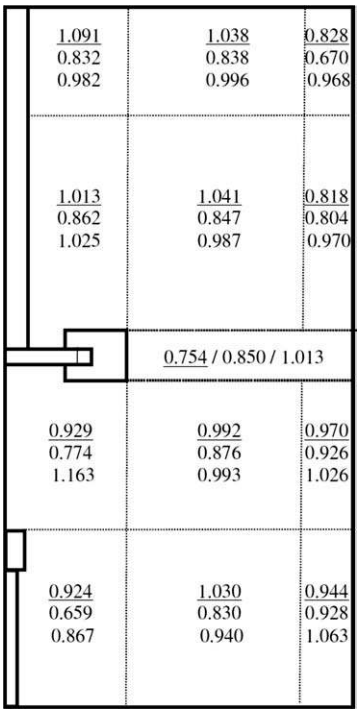

Figure 5. Local number mean diameter mm in the reactor with $N = 450$ rpm and $Q = 0.02$ vvm.

Measured data are underlined following with the predicted values from Cases 1 and 2, respectively.

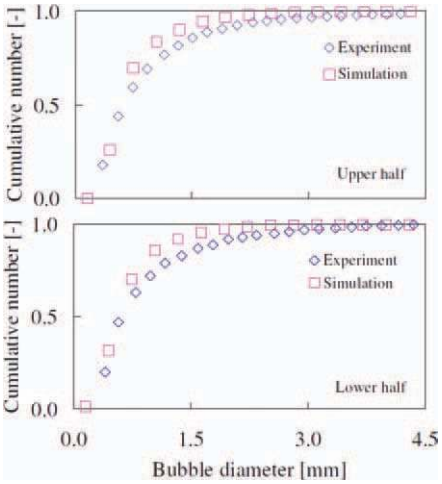

Figure 6. Cumulative distribution of bubble equivalent diameter in the upper half and lower half of the reactor with $N = 450$ rpm and $Q = 0.02$ vvm.

The prediction from the simulation Case 1 is shown. [Color figure can be viewed in the online issue, which is available at wileyonlinelibrary.com.]

In Figure 9, the long-term averaged root mean square (RMS) radial and axial velocity components at various elevations are shown. The simulation and the experiment have the maximum magnitude of the RMS values at the height of the impeller ($z/T = 0.49$). Although the agreement between experiments and simulations is not as good as for the averaged velocities, the predicted RMS values have similar order of magnitude as in the experiment. However, deviations can be observed, especially near the impeller. Clearly, these deviations were due to an insufficient grid resolution used in this work. However, it is worth to repeat here that the grid resolution is restricted by the size of bubbles present in the system. That is, the h/d_p value has to be a compromise between a sufficiently fine grid resolution to capture the most energetic eddies and a sufficiently coarse grid resolution to keep the point-volume assumption valid.

The predicted instantaneous and long-term averaged velocity vector fields are shown in Figure 10. Several small and large vortices induced by a jet-like outflow from the Rushton impeller can be observed in the plot of the instantaneous flow field. These vortices interact with each other and change their size, shape, and position randomly with time. The long-term averaged velocity vector field reveals two primary liquid recirculation zones at the upper and lower part of the reactor. Two small recirculations at the upper and lower corners can be also noticed. Snapshots of the predicted bubble dispersion pattern from the front and top view are shown in Figure 11 and Figure 12, respectively. As can be seen, the bubbles introduced at the sparger fluctuate within a small range before they are drawn into the impeller regime. Consequently, the bubbles collide with the impeller, exchange their momentum and velocity direction, and are drawn into the vortex behind the impeller blades. Most of bubble breakup takes place in this region due to the presence of high turbulence activity. The bubbles are then dispersed following the jet-like outflow. Small bubbles tend to follow the recirculations resulting in a long residence time, while

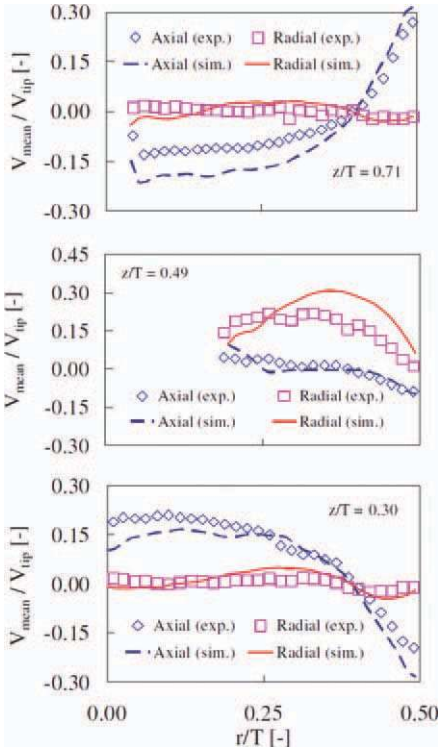

Figure 7. Experimental and predicted (Case 1) long-term averaged axial and radial liquid velocity components at three heights.

[Color figure can be viewed in the online issue, which is available at wileyonlinelibrary.com.]

large bubbles tend to rise near the wall or move into a region with low turbulence activity, that is, near the impeller shaft. These underlying phenomena and much more, such as bubble trailing and rolling of bubble swarm, can be observed in three-dimensional and anaglyphical animated results made available in the journal's website.

A contour plot of the long-term averaged resolved liquid-phase turbulent kinetic energy (TKE) at the mid-plane between baffles is shown in Figure 13. A region of high-turbulent activity, that is, high TKE, is found to emanate from the blades region and has a maximum of TKE at the midway between the impeller and the tank wall. The TKE profile is qualitatively similar to that for single phase flows (e.g., see Ref. 3). It can be concluded that the TKE is only weakly modified by the presence of bubbles due to the relatively low gas flow rate investigated here.

A simulation of a single-phase stirred tank (Case 3) was carried out to study the effect of bubbles on the liquid flow field. The predicted single-phase long-term averaged velocity vector field is shown on the left side of Figure 14. For the investigated range of the gas flow rate, no significant changes in liquid flow field are observed. More details can, however, be deduced by subtracting the averaged vector field obtained from the simulation with gassing (Case 1) from the field without gassing (Case 3). The result is shown on the right side of Figure 14. As can be seen, most of the differences take place in the outflow of the impeller region, where the liquid motion is modified by the bubbles. Our observation agrees qualitatively well with the result obtained from the experiment of Montante et al.[11] However, it should be noted that the magnitude of the difference is approximately one order of magnitude lower than the averaged flow field.

In another set of simulations, the gas flow rate was increased from 0.02 to 0.05 and 0.07 vvm in Cases 4 and 5, respectively, to investigate the effect of gassing on the gas–liquid hydrodynamics. The initial bubble diameter was assumed to 4 mm in all cases. Figure 15 shows the predicted local number mean diameter obtained from the simulations with various gas flow rates. At all gas flow rates, the evolution of the bubble size follows a similar trend as discussed in the previous section. However, it can be noticed that the increase of the gas flow rate results in a smaller mean bubble diameter in most parts of the reactor. Significant changes occurred when the gas flow rate was increased from 0.02 to 0.05 vvm. The difference between the flow rate of 0.05 and 0.07 vvm was minor. An explanation can be provided by the help of the contour plot of the phase-averaged gas volume fraction shown in Figure 16. (It should be noted that the plot of the gas fraction was made by mapping the bubble's volume based on its position on the Lagrangian frame of reference to its nearest Eulerian grid node). A significant increase in the concentration and the dispersion area of the gas phase can be observed by raising the flow rate from 0.02 to 0.05 vvm. In the first case, the dispersion pattern, that is, the gas volume fraction contour, is divided into three regimes: impeller outflow, upper, and lower recirculation zones. This is because the bubbles are only dispersed from the impeller but the recirculations are not strong enough to draw the bubbles back in the impeller regime. In contrast, the dispersion pattern for 0.05 vvm is completely connected. Thus, the bubbles are recirculating into the impeller outflow region. Consequently, more breakup takes place, resulting in smaller bubble diameters. An increase of the flow rate from 0.05 to 0.07 vvm does not qualitatively change the picture and results mainly in an increase of the concentration of the gas

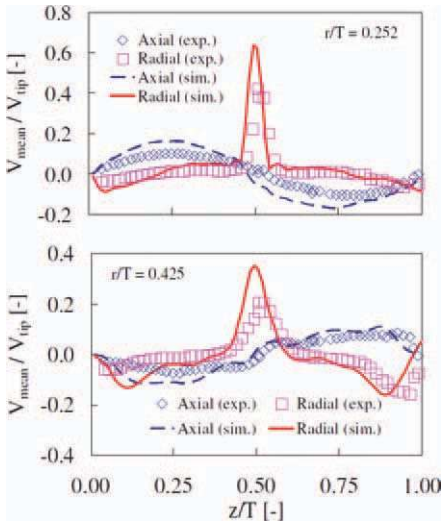

Figure 8. Experimental and predicted (Case 1) long-term averaged axial and radial liquid velocity components at two radial distances.

[Color figure can be viewed in the online issue, which is available at wileyonlinelibrary.com.]

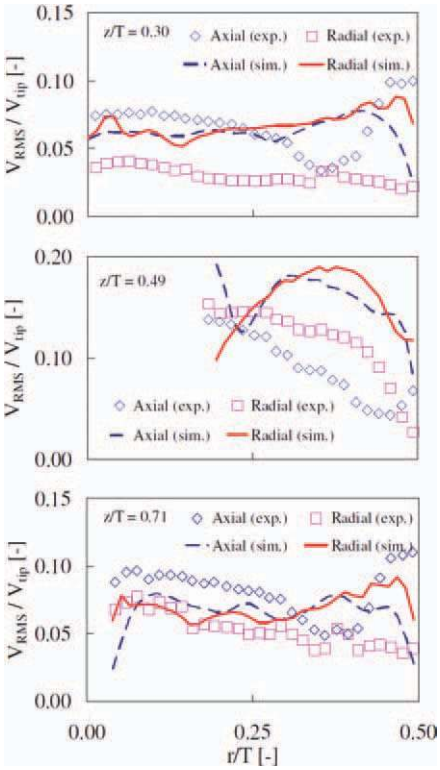

Figure 9. Experimental and predicted (Case 1) long-term averaged axial and radial fluctuating components at three heights.

[Color figure can be viewed in the online issue, which is available at wileyonlinelibrary.com.]

phase, especially in the regime near the impeller. The mean diameter of bubble changes only significantly in the regimes near the impeller shaft, where a higher rate of bubble coalescence occurs. Note that a different trend of the mean diameter will be obtained in experiments. This is because, as discussed in the previous section, the BSD at the sparger increases significantly with the gas flow rate and, consequently, the BSD in the reactor.

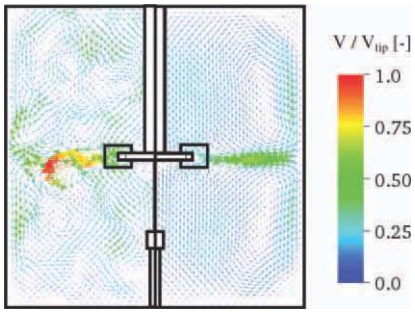

Figure 10. Predicted instantaneous (left) and long-term averaged (right) liquid velocity vector field at the mid-plane between baffles obtained from Case 1.

[Color figure can be viewed in the online issue, which is available at wileyonlinelibrary.com.]

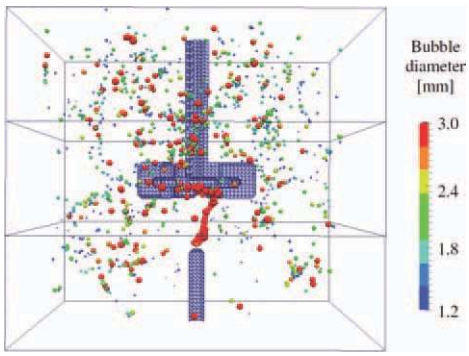

Figure 11. Snapshot of bubble dispersion pattern.

The reactor operates at $N = 450$ rpm and $Q = 0.02$ vvm. Note that the impeller and the sparger geometry are only an interpolated contour plot. The baffles and tank wall are excluded for visualization purpose. [Color figure can be viewed in the online issue, which is available at wiley onlinelibrary.com.]

Conclusions

A modeling technique for the simulations of gas–liquid stirred tank reactors based to an EL approach has been presented. The turbulent flow field was established using the filtered conservation equations. A variation of the LB scheme proposed by Somers[17] was used to discretize the equations. The bubble parcel concept was used to represent a group of bubbles with identical properties. A point-volume concept was used to track the trajectory of the bubble, that is, the parcel. A set of appropriate correlations for the interphase closure was carefully chosen from the literature. The immersed boundary condition method[22] was used to describe the action of the moving components and the tank walls.

The restriction regarding the grid size over bubble diameter ratio, h/d_p, was relaxed. It was demonstrated that the use of a h/d_p value less than unity (but greater than 0.5) can be used in EL simulations. This approach can be envisioned as a ''distributed'' bubble approach, where bubbles are allowed to be slightly bigger than the grid size and represented with a more spatially distributed forces. However, the h/d_p value used in a simulation should be a compromise between a

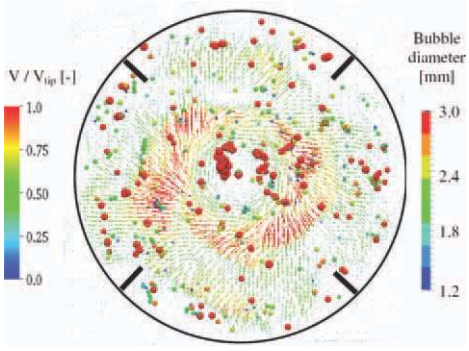

Figure 12. Snapshot of bubble dispersion pattern and the liquid velocity vector field at cross-section below the impeller.

The reactor operates at $N = 450$ rpm and $Q = 0.02$ vvm (only bubbles below the impeller are shown). [Color figure can be viewed in the online issue, which is available at wileyonlinelibrary.com.]

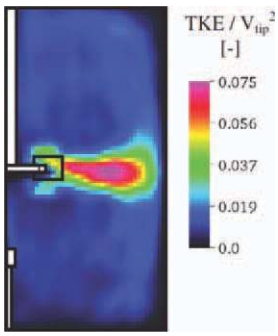

Figure 13. Contour plot of the predicted long-term averaged turbulent kinetic energy TKE for Case 1.

[Color figure can be viewed in the online issue, which is available at wileyonlinelibrary.com.]

sufficiently fine grid resolution to capture the most energetic eddies and a sufficiently coarse grid to keep the point-volume assumption valid. It should be noted that this resolution limitation will largely disappear when a simulation of an industrial-scale reactor is considered. As an increase in the reactor size will typically result in only slightly larger bubbles, finer grids (relative to the reactor size) will have h/d_p ratios greater than one.

Collisions and coalescence of bubbles were modeled based on the stochastic interparticle collision model as used by Sommerfeld et al.[27] Using the coalescence model, a good agreement between the predicted and measured BSD in a bubble column has been obtained. Simulations with various initial bubble sizes and gas flow rates showed that the accuracy of the prediction is highly sensitive to the initial bubble size at the sparger. Therefore, detailed information concerning bubble size (or air inlet/sparger) is essential for an accurate prediction.

The breakup model of Luo and Svendsen[28] was used. In this work, breakup of bubble was treated as a stochastic event. A daughter size was randomly selected from a U-shape distribution. Accordingly, breakup of bubbles was decided by comparing a breakup frequency with a uniform random number. Additionally, in this work, we proposed that this event should be bounded by an involved time scale, which is a function of the flow field, that is, the particle–

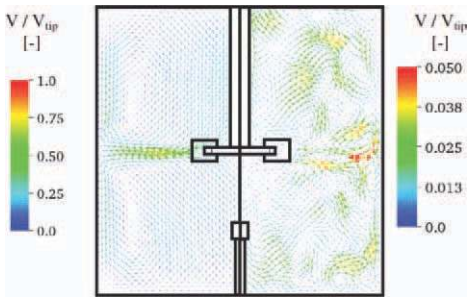

Figure 14. Vector plot of long-term averaged velocity field for ungassed conditions (Case 3; left) and the difference between the liquid velocity for gassed (Case 1) and ungassed conditions (Case 3; right).

[Color figure can be viewed in the online issue, which is available at wileyonlinelibrary.com.]

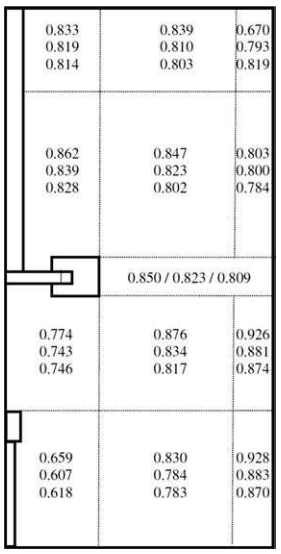

Figure 15. Local number-mean diameter (mm) in the reactor at the gas flow rate of (from top to bottom) 0.02, 0.05, and 0.07 vvm, respectively.

The impeller rotational speed was fixed at 450 rpm. [Color figure can be viewed in the online issue, which is available at wileyonlinelibrary.com.]

eddy interaction time, to obtain time resolution-independent solution and to avoid unphysical consecutive breakups.

Our modeling technique was then used to simulate gas–liquid flow in a stirred tank reactor following the experiments of Montante et al.[11,12] The simulations were able to reproduce the trends and the magnitude of the local BSD from the experiment. Small bubbles were overpredicted. This could be improved by using alternative daughter bubble-size distributions. Also, despite a coarse grid spacing used in this work, the simulations provided a good agreement with measured data for the long-term averaged velocity components. This is because the scale of large energy-containing eddies in a stirred reactor is of similar size as the impeller diameter. Therefore, the largest part of the energy in the liquid flow field was resolved. However, due to the restriction of the choice of the grid spacing, the predicted second-order statistics (RMS of velocity components) agree only by order of magnitude with the measured data. To improve the prediction of the second-order statistics, an alternative approach, such as very-large-eddy simulations (VLES), may be used. The VLES approach uses a spatial-filtering process with a turbulence model (similar to that for unsteady Reynolds-averaged Navier–Stokes approach) on a coarse grid to resolve a minor part of the turbulence spectrum and to model the rest.[45,46] It should be also pointed out that, in a gas–liquid reactor with dense dispersion regime (i.e., a global gas phase above 10% volume fraction), the gas void fraction has a significant effect on the flow field and should be included in the conservation equations. Additionally, in the dense dispersion regime, large amount of bubbles tend to accumulate and coalesce in the low-pressure region behind the impeller blades resulting in ventilated cavity.[47] To accurately model a reactor within this regime, the phase-averaged conservation equations and a hybrid approach for the modeling of the dispersed phase, for example, the hybrid two-fluid/discrete element method introduced by Sun et al.,[47] may be used. We are working on these improvements in our current research.

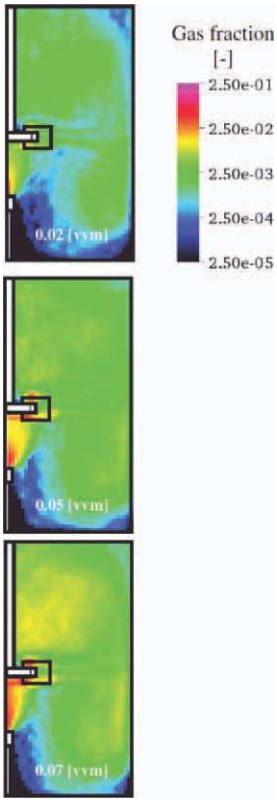

Figure 16. Long-term averaged gas volume fraction at the mid plane between baffles at gas flow rate of 0.02, 0.05, and 0.07 vvm, that is, Cases 1, 4, and 5, respectively.

[Color figure can be viewed in the online issue, which is available at wileyonlinelibrary.com.]

Bearing in mind the capabilities and limitations of the presented modeling technique, the effects of the bubble phase and the gas flow on the gas–liquid were studied numerically. It can be concluded that the presence of bubbles, in the investigated range of operating conditions, slightly modifies the flow at the impeller outflow region. Furthermore, it has been found that the increase of the gas flow rates triggers a change in the dispersion pattern and, consequently, the BSD.

Although the study presented here has been carried out for laboratory scale reactors with dilute dispersions, the present modeling technique consists mainly of models based on elementary physical principles, which are also valid for a larger scale. The models contain only a few adjustable parameters: only some rooms exists for adopting different closures and for using different theoretical constants. It should be also stressed, that all elements of the present modeling technique provide high efficiency for parallel computing, as has been demonstrated by Derksen and Van den Akker[3] and Sungkorn et al.[21] The maximum benefit of the present modeling technique can be achieved when industrial large-scale simulations are realized.

Notation

C = clearance between the impeller disc and the reactor bottom, m
c_f = increase coefficient of surface area calculated in Eq. (17)
C_S = Smagorinsky constant (set to 0.10)
d = diameter, m
D = impeller diameter, m
F = force, N
f_{BV} = breakage volume fraction calculated in Eq. (16)
g = gravitational acceleration (set to 9.82), m/s^2
h = grid cell size, m
H = liquid-filled level, m
h_0 = initial film thickness to be used in Eq. (10), m
h_f = final film thickness before rupture to be used in Eq. (10), m
N = impeller rotational speed, rev/s
r,R = radius, m
S = rate of deformation tensor to be used in Eq. (1), 1/s
T = reactor diameter, m
t,τ = characteristic time, s
u = velocity, m/s
V = volume, m^3
x = position
α = coefficient of restitution (set to 0.90)
Δ = filter width to be used in Eq. (1), m
ε = energy dissipation rate, m^2/s^3
λ = eddies length scale, m
ν = kinematic viscosity, m^2/s
ρ = density, kg/m^3
ζ = mapping function calculated from Eq. A1
σ = surface tension, N/m
Ω = rotational speed, rad/s
Ω_B = breakup rate calculated in Eq. (15), 1/s

Subscripts

eff = effective
fict = fictitious
l = continuous liquid phase
n = normal direction
new = properties after collision, coalescence, or breakup
old = properties before collision, coalescence, or breakup
p = dispersed bubble phase
t = turbulence involved properties
θ = tangential direction

Dimensionless numbers

Eo = Eötvös number = $(\rho_1-\rho_p)|\mathbf{g}|d_p^2/\sigma$
Re_p = particle Reynolds number = $|\mathbf{u}_p-\mathbf{u}|d_p/\nu_1$

Literature Cited

1. Arlov D, Revstedt J, Fuchs L. Numerical simulation of gas-liquid rushton stirred reactor—LES and LPT. *Comput Fluids*. 2008;37:793–801.
2. Gogate PR, Beenackers AACM, Pandit AB. Multiple-impeller systems with a special emphasis on bioreactor: a critical review. *Biochem Eng J*. 2000;6:109–144.
3. Derksen JJ, Van den Akker HEA. Large eddy simulations on the flow driven by a rushton turbine. *AIChE J*. 1999;45:209–221.
4. Crowe C, Sommerfeld M, Tsuji Y. *Multiphase Flows with Droplets and Particles*. Boca Raton: CRC Press, 1998.
5. Loth E. Numerical approaches for motion of dispersed particles, droplets and bubbles. *Prog Energy Combust Sci*. 2000;26:161–223.
6. Deen NG, Solberg T, Hjertager BH. Flow generated by an aerated rushton impeller: two-phase PIV experiments and numerical simulations. *Can J Chem Eng*. 2002;80:1–15.
7. Khopkar AR, Rammohan AR, Ranade VV, Dudukovic MP. Gas-liquid flow generated by a Rushton turbine in stirred vessel: CARPT/CT measurements and CFD simulations. *Chem Eng Sci*. 2005;60:2215–2229.
8. Zhang Y, Yang C, Mao Z-S. Large eddy simulation of the gas-liquid flow in a stirred tank. *AIChE J*. 2008;54:1963–1974.
9. Venneker BCH, Derksen JJ, Van den Akker HEA. Population balance modeling of aerated stirred vessels based on CFD. *AIChE J*. 2002;48:673–685.
10. Laakkonen M, Moilanen P, Alopaeus V, Aittamaa J. Modelling local bubble size distribution in agitated vessels. *Chem Eng Sci*. 2007;62: 721–740.

11. Montante G, Paglianti A, Magelli F. Experimental analysis and computational modelling of gas-liquid stirred vessels. *Trans IChemE*. 2007;85:647–653.
12. Montante G, Horn D, Paglianti A. Gas-liquid flow and bubble size distribution in stirred tanks. *Chem Eng Sci*. 2008;63:2107–2118.
13. Unverdi SO, Trygvvason G. A front-tracking method for viscous, incompressible multi-fluid flow. *J Comput Phys*. 1992;100:25–37.
14. Behzadi A, Issa RI, Rusche H. Modelling of dispersed bubble and droplet flow at high phase fractions. *Chem Eng Sci*. 2004;59:759–770.
15. Wu Z, Revstedt J, Fuchs L. *LES of a two-phase turbulent stirred reactor*. In: Lindborg E, editor. *Turbulence and Shear Flow Phenomena 2*. Stockholm: KTH, 2001:529–534.
16. Nemoda SDJ, Zivkovic GS. Modelling of bubble break-up in stirred tanks. *Therm Sci*. 2004;8:29–49.
17. Somers JA. Direct simulation of fluid flow with cellular automata and the Lattice-Boltzmann equation. *J Appl Sci Res*. 1993;51:127–133.
18. Smagorinsky J. General circulation experiments with the primitive equations. 1. The basic experiment. *Mon Weather Rev*. 1963;91:99–164.
19. Derksen JJ. Numerical simulation of solid suspension in a stirred tank. *AIChE J*. 2003;49:2700–2714.
20. Derksen JJ, Van den Akker HEA, Sundaresan S. Two-way coupled large-eddy simulations of the gas-solid flow in cyclone separators. *AIChE J*. 2008;54:872–885.
21. Sungkorn R, Derksen JJ, Khinast JG. Modeling of turbulent gas-liquid bubble flows using stochastic lagrangian model and lattice-Boltzmann Scheme. *Chem Eng Sci*. 2011;66:2745–2757.
22. Derksen JJ, Kooman JL, Van den Akker HEA. Parallel fluid flow simulation by means of a Lattice-Boltzmann scheme. *Lect Notes Comput Sci*.1997;125:524–530.
23. Sommerfeld M. Theoretical and experimental modeling of particulate flows, Lecture Series 2000–06. von Karman Institute for Fluid Dynamics: Belgium, April 3–7, 2000.
24. Deen N, Van Sint Annaland M, Kuipers JAM. Multi-scale modeling of dispersed gas-liquid two-phase flow. *Chem Eng Sci*. 2004;59:1853–1861.
25. Sommerfeld M, Kohnen G, Rueger M. Some open questions and inconsistencies of Lagrangian particle dispersion models. In: Proceedings of the Ninth Symposium on Turbulent Shear Flows. Kyoto, Japan, 1993; Paper No. 15-1.
26. Sommerfeld M. Validation of a stochastic Lagrangian modeling approach for inter-particle collisions in homogeneous isotropic turbulence. *Int J Multiphase Flow*. 2001;27:1829–1858.
27. Sommerfeld M, Bourloutski E, Broeder D. Euler/Lagrange calculations of bubbly flows with consideration of bubble coalescence. *Can J Chem Eng*. 2003;81:508–518.
28. Luo H, Svendsen HF. Theoretical model for drop and bubble breakup in turbulent dispersions. *AIChE J*. 1996;42:1225–1233.
29. Succi S. *The Lattice Boltzmann Equation for Fluid Dynamics and Beyond*. Oxford: Clarondon Press, 2001.
30. Chen S, Doolen GD. Lattice Boltzmann method for fluid flows. *Annu Rev Fluid Mech*.1998;30:329–364.
31. Eggels JGM, Somers JA. Numerical simulations of free convective flow using the lattice-Boltzmann scheme. *Int J Heat Fluid Flow*. 1995;16:357–364.
32. Hu G, Celik I. Eulerian-Lagrangian based large-eddy simulation of a partially aerated flat bubble column. *Chem Eng Sci*. 2008;63:253–271.
33. Derksen JJ. Assessment of large eddy simulations for agitated flows. *Trans IChemE A*. 2001;79:824–830.
34. Goldstein D, Handler R, Sirovich L. Modeling a no-slip flow boundary with an external force field. *J Comput Phys*.1993;105:354–366.
35. Van Driest ER. On turbulent flow near a wall. *J Aeronaut Sci*.1956;23:1007–1011.
36. Spalding DB. A single formula for the law of the wall. *J Appl Mech*. 1961;28:455–458.
37. Darmana D, Deen NG, Kuipers JAM. Numerical study of homogeneous bubbly flow: influence of the inlet conditions to the hydrodynamic behavior. *Int J Multiphase Flow*. 2009;35:1077–1099.
38. Tsuji Y, Tanaka T, Ishida T. Lagrangian numerical simulation of plug flow of cohesionless particles in a horizontal pipe. *Powder Technol*. 1992;71:239–250.
39. Hoomans BPB, Kuipers JAM, Briels WJ, Van Swaaij WPM. Discrete particle simulation of bubble and slug formation in a two-dimensional gas-fluidised bed: a hard-sphere approach. *Chem Eng Sci*. 1996;51:99–118.
40. Prince MJ, Blanch HW. Bubble coalescence and break-up in air-sparged bubble columns. *AIChE J*. 1990;36:1485–1499.
41. Deen NG, Solberg T, Hjertager BH. Large eddy simulation of the gas-liquid flow in a square cross-sectioned bubble column. *Chem Eng Sci*. 2001;56:6341–6349.
42. Van den Hengel EIV, Deen NG, Kuipers JAM. Application of coalescence and breakup models in a discrete bubble model for bubble columns. *Ind Eng Chem Res*. 2005;44:5233–5245.
43. Geary NW, Rice RG. Bubble size prediction for rigid and flexible spargers. *AIChE J*. 1991;37:161–168.
44. Lehr F, Millies M, Mewes D. Bubble-size distribution and flow fields in bubble columns. *AIChE J*. 2002;48:2426–2443.
45. Ruprecht A, Helmrich T, Buntic I. Very large eddy simulation for the prediction of unsteady vortex motion. In: Conference on Modelling Fluid Flow. Budapest, Hungary, 2003.
46. Fares E. Unsteady flow simulation of the Ahmed reference body using a lattice Boltzmann approach. *Comput Fluids*. 2006;35:940–950.
47. Middleton JC, Smith JM. *Gas-liquid mixing in turbulent systems*. In: Paul EL, Atiemo-Obeng VA, Kresta SM, editors. *Handbook of Industrial Mixing: Science and Practice*. New Jersey: Wiley-Interscience, 2004: 257–344.
48. Sun J, Battaglia F, Subramaniam S. Hybrid two-fluid DEM simulation of gas-solid fluidized beds. *Trans ASME*. 2007;129:1394–1403.
49. Hennick EA, Lightstone MF. A comparison of stochastic separated flow models for particle dispersion in turbulent flows. *Energy Fuels*. 2000;14:95–103.

Appendix

Mapping function

The so-called cheap clipped fourth-order polynomial mapping function is formulated as[6]:

$$\zeta(\mathbf{x}-\mathbf{x}_\mathrm{p})=\frac{15}{16}\left[\frac{(\mathbf{x}-\mathbf{x}_\mathrm{p})^4}{\mathrm{n}^5}-2\frac{(\mathbf{x}-\mathbf{x}_\mathrm{p})^2}{\mathrm{n}^3}+\frac{1}{\mathrm{n}}\right] \quad \text{with } |\mathbf{x}-\mathbf{x}_\mathrm{p}| \leq \mathrm{n}, \tag{A1}$$

with x the position of a neighboring grid node and n half of the predefined influence diameter (set to $2d_\mathrm{p}$ in this work).

Calculation of the eddy–particle interaction time

The time interval in which a bubble interacts with a randomly sampled velocity field, that is, the eddy–particle interaction time t_e is determined by the eddy lifetime t_eddy and the transit time t_tr as[49]

$$t_e = \min(t_\mathrm{eddy}, t_\mathrm{tr}). \tag{A2}$$

The eddy lifetime t_eddy is given by:

$$t_\mathrm{eddy} = \frac{l_\mathrm{eddy}}{|\mathbf{u}'|}, \tag{A3}$$

with u' the liquid phase velocity fluctuation. The dissipation length scale l_eddy is estimated by:

$$l_\mathrm{eddy} = 0.3\frac{k^{1.5}}{\varepsilon}, \tag{A4}$$

with k being the turbulent kinetic energy.

Table A1. Expressions for the Forces Acting on a Bubble

Force	Closure
$\mathbf{F}_G = \left(\rho_p - \rho_l\right) V_p \mathrm{g}$	-
$\mathbf{F}_S = \rho_l V_p D_t \mathrm{u}$	-
$\mathbf{F}_D = -\frac{1}{2} C_D \rho_l \pi r_p^2 \lvert \mathrm{u}_p - \mathrm{u} \rvert \left(\mathrm{u}_p - \mathrm{u}\right)$	$C_D = \max\left[\min\left[\frac{24}{\mathrm{Re}_p}\left(1 + 0.15\mathrm{Re}_p^{0.687}\right), \frac{48}{\mathrm{Re}_p}\right], \frac{8}{3}\frac{Eo}{Eo+4}\right]$
$\mathbf{F}_L = -C_L \rho_l V_p \left(\mathrm{u}_p - \mathrm{u}\right) \times \nabla \times \mathrm{u}$	$C_L = \begin{cases} \min\left[0.288\tanh\left(0.121\mathrm{Re}_p\right), f(Eo_d)\right], & Eo_d \le 4 \\ f(Eo_d), & 4 < Eo_d \le 10 \\ -0.29, & Eo_d > 10 \end{cases}$
	$Eo_d = \frac{Eo}{E^{2/3}}, \quad E = \frac{1}{1 + 0.163 Eo^{0.757}}$
	$f(Eo_d) = 0.00105 Eo_d^3 - 0.0159 Eo_d^2 - 0.0204 Eo_d + 0.474$
$\mathbf{F}_A = -C_A \rho_l V_p \left(D_t \mathrm{u}_p - D_t \mathrm{u}\right)$	$C_A = 0.5$

The transit time of a bubble is estimated based on the linearized form of the equation of motion of a bubble in uniform flow:

$$t_{\mathrm{tr}} = -\tau_{\mathrm{p}} \ln\left(1 - \frac{l_{\mathrm{e}}}{\tau_{\mathrm{p}} \lvert \boldsymbol{u} - \boldsymbol{u}_{\mathrm{p}} \rvert}\right), \tag{A5}$$

with the particle relaxation time τ_{p}

$$\tau_{\mathrm{p}} = \frac{\rho_{\mathrm{p}} \mathrm{d}_{\mathrm{p}}^2}{18 \rho \mathrm{v}}. \tag{A6}$$

Manuscript received Feb. 4, 2011, and revision received Apr. 20, 2011.